Advanced Functional Materials

ADVANCED FUNCTIONAL MATERIALS
www.afm-journal.de

RESEARCH ARTICLE OPEN ACCESS

Shape-Controlled Guanine Self-Assemblies for Stable and Fast-Ion Solid–Electrolyte Interphases in Sustainable Li Metal Batteries

So-Huei Kang[1,2,3] | So-Dam Sohn[4,5] | Kyung Min Lee[1] | Seok-Kyu Cho[6,7] | Byongkyu Lee[1] | Ji Eun Lee[8] | Sang-Young Lee[6] | Sang Kyu Kwak[8] | Hyung-Joon Shin[4] | Changduk Yang[1,2,9]

[1]Department of Energy Engineering, School of Energy and Chemical Engineering, Ulsan National Institute of Science and Technology (UNIST), Ulsan, Republic of Korea | [2]UNIST InnoCORE AI-Space Solar Initiative, Ulsan National Institute of Science and Technology (UNIST), Ulsan, Republic of Korea | [3]Department of Chemistry, McGill University, Montreal, Quebec, Canada | [4]Department of Materials Science and Engineering, Ulsan National Institute of Science and Technology (UNIST), Ulsan, Republic of Korea | [5]Korea Research Institute of Standards and Science (KRISS), Daejeon, Republic of Korea | [6]Department of Chemical and Biomolecular Engineering, Yonsei University, Seoul, Republic of Korea | [7]UBATT Inc., Daejeon, Republic of Korea | [8]Department of Chemical and Biological Engineering, Korea University, Seoul, Republic of Korea | [9]Graduate School of Carbon Neutrality, Ulsan National Institute of Science and Technology (UNIST), Ulsan, Republic of Korea

Correspondence: Sang-Young Lee (syleek@yonsei.ac.kr) | Sang Kyu Kwak (skkwak@korea.ac.kr) | Hyung-Joon Shin (shinhj@unist.ac.kr) | Changduk Yang (yang@unist.ac.kr)

Received: 14 December 2025 | **Revised:** 10 March 2026 | **Accepted:** 10 March 2026

Keywords: guanine | hydrogen bonding | molecular networks | scanning tunneling microscopy | side-chain engineering

ABSTRACT

Guanine (G) is a fascinating molecular tool because of its ability to create supramolecular self-assemblies; thus, G is usable in a wide range of applications. Although the shape of G self-assemblies is an important factor governing supramolecular structures and properties, its control is challenging. Herein, we demonstrate that the shapes of G self-assemblies can be tuned by introducing alkyl (G8), fluoroalkyl (G8f), and oligoether (G8g) side chains into the G moiety. Consequently, we observe an unordered scaffold for G and G8g, quartet-based assemblies for G8, and hexads-based assemblies for G8f, as evidenced by scanning tunneling microscopy and molecular mechanics calculations. In addition, the shape-varying G self-assemblies show promise as artificial solid–electrolyte interphases (SEI) for lithium (Li) metal battery electrodes, revealing enhanced mechanochemical stability and reduced SEI resistance and activation energy for charge transport, particularly for G8f-Li cells, which might result from favorable self-assembling ability and improved structural integrity. We expect the side–chain engineering of G self-assemblies may provide a useful strategy for designing artificial SEIs for Li metal batteries and related supramolecular systems because of its simplicity and versatility.

1 | Introduction

As a well-known biomolecular component of DNA, guanine (G) can form multiple intermolecular hydrogen bonds, enabling the pairing of nucleic acids and a self-assembled G structure into a ribbon-type 2D network or disk-type cyclic tetramers (G-quartets) on the surface or in solution [1–13]. The structure of G self-assemblies depends on the type of tautomer. According to the study by Zhang et al. [14]. on the tautomerization of G and G-quartet formation on the Au(111) surface using

So-Huei Kang, So-Dam Sohn, Kyung Min Lee, Seok-Kyu Cho and Byongkyu Lee contributed equally to this work.

scanning tunneling microscopy (STM), there are two most stable tautomers (the canonical G/9H and noncanonical G/7H forms, as shown in Scheme S1), which can be converted into each other by increasing the temperature (converting G/9H to G/7H form) or adding a sodium source (i.e., sodium chloride) on the monolayer formed on the Au(111) surface and heating the resulting mixture (converting G/7H to G/9H form). The G in the G/9H form can constitute a G-quartet with the aid of a cation when hydrogen bonding occurs at N1H•••O6 and N2H•••N7; however, without cations, G adsorbs in a disordered manner. The noncanonical G/7H form can constitute a ribbon-type 2D network with hydrogen bonding at N2H•••N9, N1H•••N3, and O6•••N2H. Unlike a ribbon-type 2D network, the G-quartet aggregates further into a supramolecular self-assembled structure called G-quadruplexes through π–π stacking. When a G-quartet/G-quadruplex is formed, voids are generated at the G-quartet/G-quadruplex center, which can be used in various applications [15–19], such as molecule separation/storage, proton/charge conduction, luminescence and molecular sensing, catalysis, and chiral separation, similar to other porous materials.

Incorporating side chains not only affects intermolecular hydrogen bonding, but also changes polarity, bulkiness, and intermolecular interactions at the side-chain-substituted position, which may not directly contribute to the hydrogen bonding properties of G molecules but may influence the molecular arrangement. Among the various side chains, commonly used alkyl chains enhance the solubility of molecules in organic solvents and impart hydrophobicity to molecules [20, 21]. In contrast, oligoether chains exhibit a relatively hydrophilic properties enhancing molecular affinity to water- and alcohol-based solvents, high flexibility enabling free rotation of the side chains and closer stacking of molecules, and low glass transition temperatures due to ether groups [22–27]. Fluoroalkyl chains exhibit low friction coefficients, high rigidity, hydrophobicity, lipophobicity, extremely low surface energy, chemical inertness, and thermal resistance [28–31]. In particular, the lipophobicity of fluoroalkyl chains enhances the self-assembly of molecules in a solid state [20].

In this study, we designed and prepared G-based molecules possessing three types of side chains with different polarities and characteristics (alkyl, fluoroalkyl, and oligoether) to determine their roles in the arrangement of G molecules and the formation of hydrogen bonds between them, where they were designated as G8 (G with an alkyl chain), G8f (G with a fluoroalkyl chain), and G8g (G with an oligoether chain) (Figure 1a). The molecular arrangements of G and its derivatives, which were thermally deposited on the Au(111) surface, were investigated by STM. In addition, the interaction energies of G and its derivatives in several unit models were investigated using molecular mechanics calculations to explain the effect of side chains on the molecular arrangement. Finally, we demonstrate their applicability as a class of artificial solid-electrolyte interphase (SEI) for sustainable lithium (Li) metal battery electrodes. In principle, SEIs are electronically insulating but ionically conductive thin protective layers, which contribute to the electrochemical reliability of resulting batteries by suppressing unwanted interfacial side reactions between electrodes and electrolytes [32, 33]. Therefore, a mechanochemically stable SEI capable of facilitating Li transport is urgently required for long-cyclable Li electrodes. In addition to conventional SEIs formed via electrochemical reactions between anodes and electrolytes, artificial SEIs have gained considerable attention as a practical and straightforward alternative to alleviate the direct exposure of Li to electrolytes [34, 35]. The thermally deposited artificial G-based SEIs, which can form highly ordered self-assembled structure and π-stacked layers, enhanced mechanochemical stability of SEI on Li electrode and lowered SEI resistance and activation energy for charge transport, which is consistent with previously reported results [36]. We note that the improved electrochemical performance of the Li electrodes was achieved by introducing a 100-nm-thick artificial SEI. Among the tested cells, the G8f-Li-based cell exhibited the best device performance in terms of ion transport and mechanochemical stability owing to the strong tendency to form self-assembled structure and enhanced structural integrity. Our study provides a simple method for controlling the shape of G-based self-assemblies and self-assembling ability, which should improve their applications.

2 | Results and Discussions

2.1 | Synthesis and Characterization

G-based molecules were prepared by following the synthesis procedures outlined in Schemes S2 and S3. 2-Amino-6-chloropurine (**1**) was first alkylated using three different side chains, and the sequential hydrolysis of the alkylated purines using trifluoroacetic acid and water afforded the target G derivatives. The purity and structures of the intermediates and target molecules were verified by ^{1}H and ^{13}C NMR spectroscopy, matrix-assisted laser desorption/ionization time-of-flight (MALDI-TOF) mass spectrometry, and elemental analysis. The synthesis details and structural characterization results are provided in the Synthesis section of Supporting Information. All G-based molecules are white powders and dissolve easily in high-polarity solvents, such as dimethyl sulfoxide and *N,N*-dimethyl formamide, but exhibit limited solubility in other organic solvents, such as chloroform, dichloromethane, tetrahydrofuran, acetone, methanol, and acetonitrile.

2.2 | Thermal Properties

The thermal properties of the G derivatives were determined by thermogravimetric analysis (TGA) and differential scanning calorimetry (DSC) (Figures S1 and S2). According to the TGA results, the decomposition temperatures (T_d) of the molecules are 449°C (G), 345°C (G8), 322°C (G8f), and 339°C (G8g) (Figure S1), indicating that these materials exhibit sufficient thermal stability for thermal deposition at high temperatures and device fabrication for the various applications mentioned above. The higher T_d value of G than those of G derivatives may result from the larger number of hydrogen-bonding sites. According to the DSC curves in Figure S2, there are no obvious exothermal and endothermic events for the G moiety in the temperature range of 0°C–350°C, whereas G8, G8f, and G8g exhibit melting points (T_m) of 278°C, 266°C, and 226°C upon heating, respectively, in addition to several other endothermic events. The remarkably lower T_m of G8g can be attributed to the increased flexibility of

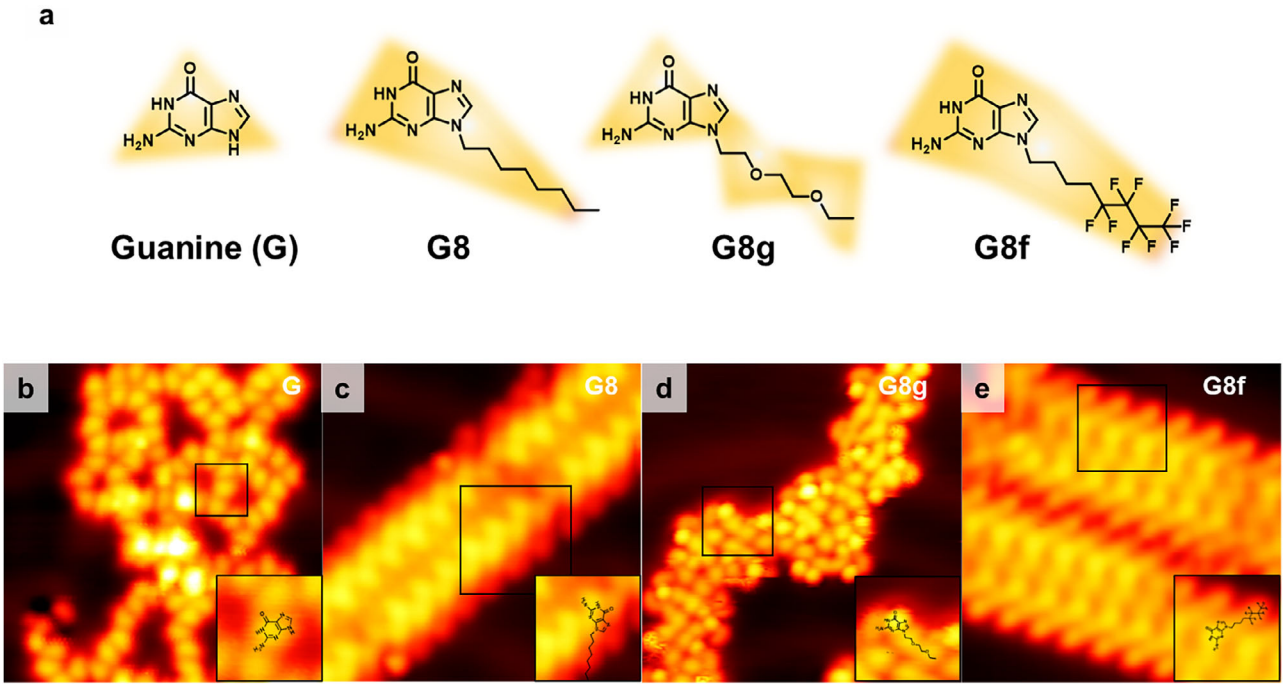

FIGURE 1 | Adsorption of guanine and its derivatives at low coverage. (a) Chemical structures of G and its derivatives possessing three types of side chains (alkyl chains, fluoroalkyl chains, and oligoether chains). (b–e) STM images of (b) G, (c) G8, (d) G8f, and (e) G8g on Au(111) surface at a low coverage in 10 nm × 10 nm scale. The self-assembled structure of G8 and G8f show ribbon structures (G8-R1 and G8f-R1). The inset in (b–e) shows a close-up view of each molecule.

the oligoether chain induced by the ether linkages. During the cooling cycle from the melted state, exothermic crystallization peaks appeared at 216°C for G8, 253°C for G8f, and 185°C and 124°C for G8g. These results demonstrate that introducing fluorine substituents in G8f makes it more crystalline compared to G8 and G8g, which is attributed to the interdigitation of the side chains.

2.3 | Scanning Tunneling Microscopy Analyses

The molecular interactions of the G-based molecules were observed by STM (Figures 1 and 2). In early studies, G was found to form a quartet through self-assembly [37]; however, it was later revealed that G forms quartet structures in which four G moieties centered around a cation only in the existence of cations [14, 38]. We obtained STM images in which G is randomly adsorbed on Au(111) at low coverage (Figure 1b). The appearance of each G derivative in the STM images is inferred from the triangular shape of G, which is highlighted against a yellow background in Figure 1a. G8 and G8f appear as a triangular shape with a long tail that is distinguished from the G moiety without a side chain and are assembled in the form of a ribbon with a long-range order (R1 in Scheme S4), whereas G8g appears as zigzag-shaped lobes in a randomly assembled structure (Figure 1c–e). The alkyl and fluoroalkyl side chains attached to the G moiety in G8 and G8f, respectively, could prohibit hydrogen bonding at the N9 position but promote lamellar interactions between the side chains and allow hydrogen bonding at N7, O6, N1H, and N2H, thereby enabling the molecules to be adsorbed onto the Au(111) surface in ribbon-type 2D structures. In contrast, the oxygen atoms of the oligoether side chain in G8g, which are expected to form hydrogen bonds with the hydrogen atoms of the G moiety, disrupt the formation of an assembled structure with a long-range order. As shown in the STM images in Figure 1b–e, all molecules are assembled on the Au(111) surface without exhibiting a preferential orientation with respect to the Au(111) surface or changing the underlying herringbone pattern of close-packed Au(111), which typically undergoes a $22 \times \sqrt{3}$ reconstruction when molecules are chemisorbed [39].

At higher (medium) coverage, G (ref. [14]) and G8g (Figure S3) still exhibited randomly adsorbed structures even though the intermolecular interaction could change. In contrast, the ribbon-shaped islands in the R1 structure assemble, as if the zippers are closed at a medium coverage (Figure 2a,b), forming a new, larger 2D ribbon structure in which the molecules are parallel to each other (R2 in Scheme S4). The herringbone pattern of the Au surface underneath each molecular layer remains unperturbed upon additional molecular adsorption, demonstrating the strong self-assembling ability of G8 and G8f on the Au surface without inducing herringbone reconstruction of the Au surface. Our results show that the intermolecular interactions have a stronger effect on the self-assembled structures than the molecule–substrate interactions of G and its derivatives with Au surface. In this case, the relationship between diffusivity and the number of deposited molecules on the substrate is expected to affect the self-assembled structures. As the coverage of G8 increased, slightly denser 2D ribbon networks appeared (Figure 2c, R3 in Scheme S4). The different ribbon adsorption structures of G8 at medium and full coverage on Au are denoted as G8-R2 and G8-R3, respectively. By transition of G8 in the adsorbed structure from R2 to R3, the density of molecules on the surface increased from 0.9 to 1.1 molecules nm^{-2}. The unit cells of G8 and G8f

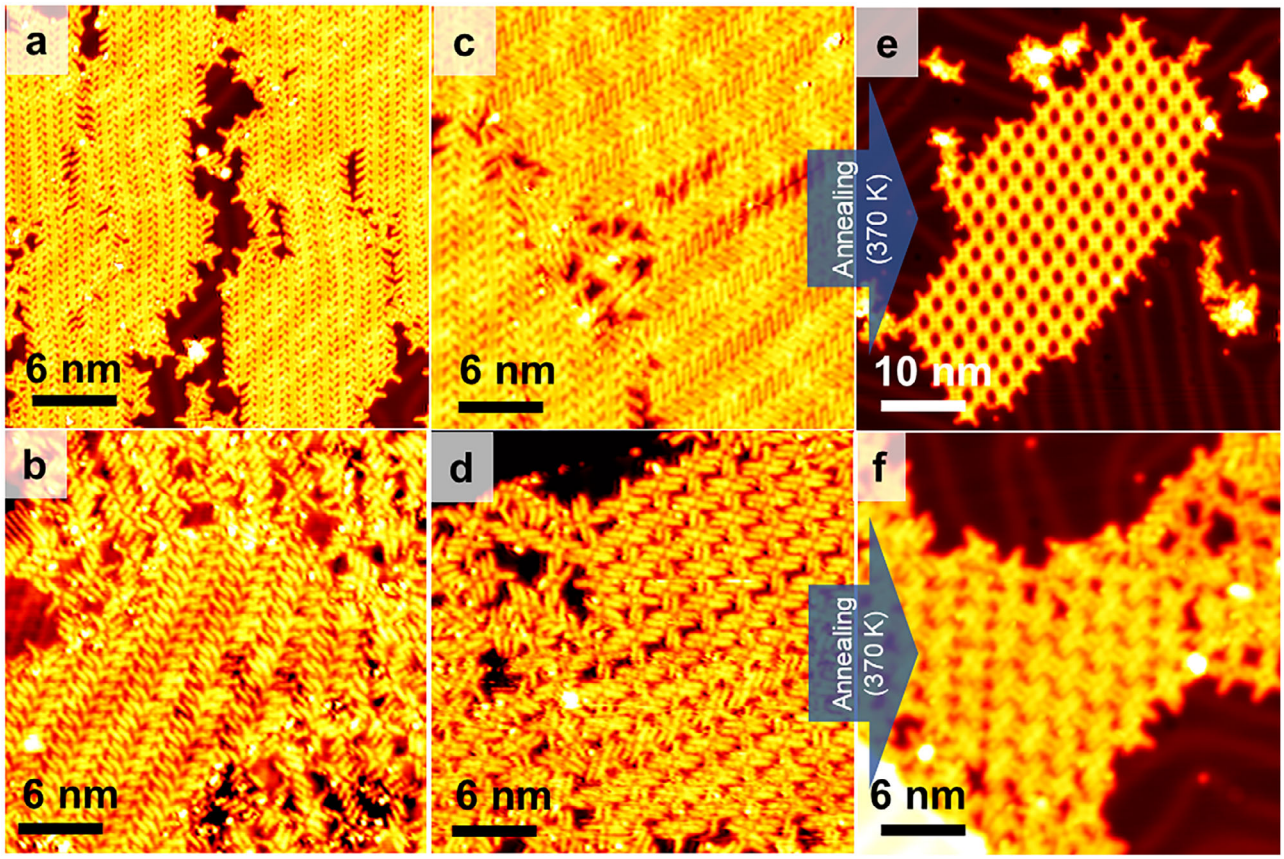

FIGURE 2 | Adsorption of G8 and G8f with increasing coverages and temperature. (a–d) STM images of (a) ribbon structures of G8 (G8-R2) and (b) G8f (G8f-R2) at the 0.8 molecular layer (at a medium coverage) and (c) ribbon structures of G8 (G8-R3) and (d) hexad structures of G8f (G8f-H) at full coverage. (e,f) STM images of (e) quartet structures of G8 (G8-Q) and (f) hexad structures of G8f (G8f-H) after annealing at 370 K.

superstructures and their unit cell parameters are provided in Figure S4 and Table S1, respectively. When the Au substrate with G8-R3 was annealed at 370 K, some G8 molecules are desorbed from the surface, overcoming the van der Waals interactions between G8 and the substrate. The G8 molecules on the surface underwent a phase transformation to the most stable a quartet structure (G8-Q) (Figure 2e). The alkyl side chain hinders the tautomerization of G8 from the G/9H to the G/7H and proton tunneling via thermal annealing, which promotes the formation of a stable quartet structure of the G/9H. In contrast, as the coverage of G8f increases from medium to full coverage, the self-assembled adsorption structure changes from ribbon (G8f-R2) to hexad (G8f-H), thereby increasing the density of molecules on the surface from 0.9 to 0.98 molecules nm^{-2} (Figure 2b,d and Table S1). When more G8f molecules adsorb onto G8f-R2, the strong intermolecular interaction between G8f molecules allows them to overcome the energy barrier of changing the intermolecular binding sites between them, forming a denser hexagonal form rather than stacking on the existing G8f-R2 layer. The hexad structure of G8f-H is maintained after thermal annealing at 370 K (Figure 2f), despite the applied thermal energy being sufficient to desorb some G8f molecules from the Au substrate. No further transformation is observed in the adsorption structure, as the transformation energy to form other structures may be higher than the desorption energy of G8f-H from the Au substrate.

2.4 | Theoretical Calculations

To elucidate the transitions of the adsorption structures of G8 and G8f on the Au(111) surface upon coverage changes, the thermodynamic stabilities of the adsorption structures were investigated via molecular mechanics simulations. We explored the formation energy (ΔE_{for}) values of the receptive G8- and G8f-based unit cells inferred from the STM data to compare their thermodynamic stabilities as follows:

$$\Delta E_{for} = \frac{\Delta E_{tot} - \Delta E_{Au} - n\Delta E_{G}}{n}$$

where ΔE_{tot} denotes the total energy of the system, ΔE_{Au} denotes the energy of the Au(111) surface, n denotes the number of G derivative molecules adsorbed on the Au(111) surface, and ΔE_{G} denotes the energy of the G derivative molecules in a vacuum. Here, to properly assess the theoretical data corresponding to the STM results above, we calculated the ΔE_{for} values at a 6×6 supercell (considered medium coverage) and a fully expanded supercell to cover all Au(111) surfaces (considered full coverage) (Computational Details and Figure S5).

For the G8-based supercell at a medium coverage, the G8-R2 exhibited the lowest ΔE_{for} value of (–1598.3 kJ mol^{-1}), explaining the dominance of the less dense G8-R2 adsorption structure

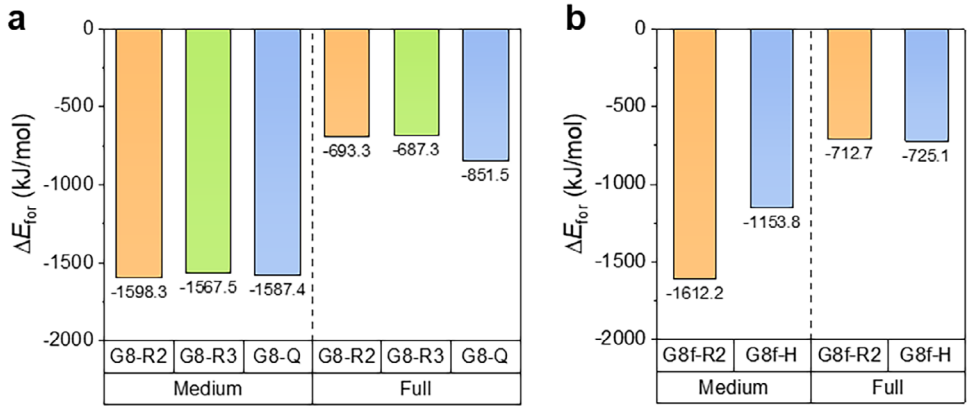

FIGURE 3 | Thermodynamic stability of adsorption structures. Formation energy of (a) G8 and (b) G8f adsorption structure on Au(111) surface upon the coverage change.

(Figure 3a). In contrast, at full coverage, the ΔE_{for} of the denser G8-Q adsorption structure was 1.23 times more negative than that of G8-R2, indicating a significant change in the order of thermodynamic stability upon an increase in the adsorption coverage and suggesting G8-Q as the most stable and favorable adsorption structure. However, according to the STM results, when the coverage of G8 was increased from medium to full coverage, G8-R2 was converted to G8-R3 with a denser 2D ribbon network rather than G8-Q to accommodate the increased number of molecules on the substrate despite the slightly lower thermal stability of G8-R3 than G8-R2 at full coverage, and a post-treatment (thermal annealing) was required to form the G8-Q structure. It is speculated that the energetic barrier to the conversion of G8-R2 to G8-Q at full coverage is too large to promote the direct transition of G8-R2 to G8-Q without thermal annealing. Similarly, the tendency of ΔE_{for} upon coverage changes also explains the adsorption structure transition of the G8f-based supercell (Figure 3b). At medium coverage, the ΔE_{for} of the G8f-H structure is only approximately 72% of that of the G8f-R2 ribbon structure, which leads to the formation of a more stable ribbon structure. However, at full coverage, the ΔE_{for} of G8f-H is more negative than that of the G8f-R2 structure. Thus, G8f-H is expected to exhibit a more favorable adsorption structure at full coverage, as observed in the STM results. Accordingly, we confirmed that the coverage dependence of the preferred adsorption structure originates from the order of the thermodynamic stability of the adsorption structures.

2.5 | Thin-Film Microstructural Analyses

After learning that G and its derivatives exhibit interesting self-assembly properties and that their adsorption structures on Au(111) are significantly influenced by their coverage and thermodynamic stability, we investigated the self-assembled structures of G and its derivatives for applications in devices, such as Li(100) surface in Li batteries.

At first, we prepared thin films thermally deposited on Li/Cu surface (under a high vacuum of 1.5×10^{-6} torr and at moderate temperatures in the range of 180°C–200°C) and tried 2D grazing incidence X-ray diffraction measurement. However, due to the low stability of Li at high moisture and oxygen levels outside the glove box, the samples were significantly damaged outside the glove box, and it was difficult to analyze the self-assembled structure or thin-film properties of G and G derivatives on Li surfaces. Instead, thin films of G and its derivatives thermally deposited on silicon substrate at the same condition were analyzed by 2D grazing incidence X-ray diffraction (Figure 4). The films of G, G8, G8g, and G8f exhibit π–π stacking peaks at approximately $2\theta = 26.9°$, 22.6°, 24.4°, and 22.8°, respectively, along the out-of-plane direction ($2\theta_z$), corresponding to d-spacing ($d_{\pi-\pi}$) values of 3.3, 3.9, 3.6, and 3.9 Å, indicating the formation of highly ordered π-stacked layers of G derivatives with a face-on dominant orientation relative to the substrate. The $d_{\pi-\pi}$ value of G (3.3 Å) increases to 3.6–3.9 Å of the G derivatives owing to the side chains. The smaller $d_{\pi-\pi}$ of G8g (3.6 Å) than those of G8 (3.9 Å) and G8f (3.9 Å) can be attributed to the higher flexibility of the oligoether chain. In contrast, lamellar stacking peaks of the side chains appear for G8, G8g, and G8f with d-spacing ($d_{lamellar}$) values of 7.9, 7.2, and 7.6 Å, respectively. The variation in $d_{lamellar}$ can be attributed to the different bulkiness of the side chains and the different strengths of the intermolecular interactions between them. The flexibility of the oligoether chain and the smaller atomic size of oxygen than that of carbon can reduce the $d_{lamellar}$ of G8g compared with that of G8. In contrast, the strong intermolecular interactions between the fluoroalkyl chains slightly reduced the $d_{lamellar}$ of G8f compared to G8. Based on the above findings, G and its derivatives appear to construct highly ordered π–stacked layers with strong interactions between the side chains.

To investigate the self-assembled structure of G8 and G8f on Li(100) surface, the thermodynamic stability of G8 and G8f adsorption structures on the Li(100) surface was investigated via molecular mechanics simulations, as similarly performed on the Au(111) surface (Figure S8). The ΔE_{for} values of the adsorption structure differ from those on the Au(111) surface, but G8 and G8f may thermodynamically favor G8-Q and G8f-H configurations on Li(100) surface with the lowest ΔE_{for} values, respectively.

To investigate the self-assembled structure would maintain the hexad motif when they stack, we compared the STM images and of the corresponding fast Fourier transform (FFT) of G8f monolayer and multilayer films (Figure S9). The STM image of the G8f monolayer reveals a periodic arrangement of hexad motifs (Figure S9a), and the corresponding FFT (Figure S9b) exhibits

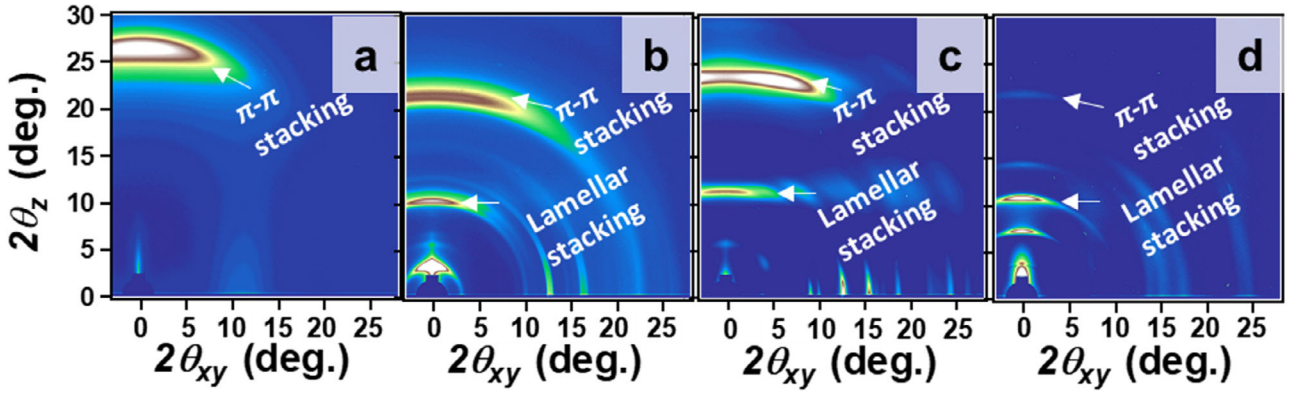

FIGURE 4 | Microstructure of a thin film of G and its derivatives. 2D-GIXD images of thermally deposited (a) G, (b) G8, (c) G8g, and (d) G8f on silicon substrate.

two types of major peaks, α from the motifs and β from their long-range arrangement. The inverse fast Fourier transformed images (Figure S9c,d) clearly show these periodicities in the STM image. The multilayer film (Figure S9f–j) is composed of multiple grains, which exhibit the same periodic arrangement of hexad motifs as that of monolayer. These results show that the hexad motifs and their long-range arrangement are preserved in the multilayer, although the orientations vary from domain to domain.

2.6 | Applicability as an Artificial Solid–Electrolyte Interphase

The potential application of a thin layer of G and its derivatives as an artificial SEI was explored. As a proof-of-concept, a thin layer of G and its derivative-based artificial SEI was fabricated on top of a Li foil (see details in Experimental Section). The electrochemical performance of the SEI-Li|SEI-Li and Li|Li symmetric cells was examined by galvanostatic Li plating and stripping cycle tests at a current density and capacity of 1 mA cm^{-2} and 1 mAh cm^{-2}, respectively (Figure 5a). The bare Li cell (Li|Li cell) exhibited irreversible voltage fluctuations with a large overpotential and failed after 150 h. With the SEI layers of G8g (G8g-Li) and G8 (G8-Li), cyclability improved; however, these cells failed after 300 h. This result indicates that the mechanochemical stability of the G8g- and G8-based artificial SEIs is insufficient to prevent the continuous consumption and depletion of electrolytes, resulting in the accelerated formation of dead Li [40, 41]. In contrast, the G8f-Li cell exhibits a modest increase in overpotential but reliable Li plating and stripping cyclability over 400 h, demonstrating the mechanochemical robustness of G8f-based artificial SEIs.

This clear dependence on structural integrity was further investigated by electrochemical impedance spectroscopy after the cycle test (Figure 5b and Table S2). All artificial SEI-containing cells exhibit lower SEI (R_{SEI}) and charge transfer (R_{CT}) resistances than those of bare Li. G8f-Li exhibits the lowest R_{SEI} and R_{CT} (7.59 and 28.1 Ω, respectively). Arrhenius plots of R_{SEI} and R_{CT} were examined to estimate the activation energy (E_a) of charge transport through the electrolyte–SEI interface and SEI (Figure 5c and Table S2). Regardless of their components, the artificial SEI (G8g, G8, and G8f)-containing cells exhibited similar energy barriers to each other (≈0.30 eV for the E_a of R_{CT} and ≈0.11 for the E_a of R_{SEI}).

These results suggest that artificial SEI-containing Li may have similar electrochemical behavior. The most notable finding is that the artificial SEI exhibits a lower E_a of R_{SEI} than bare Li (0.18 eV). When we compared the initial (before cycle) and final (after cycle) impedance data, the artificial SEI-containing cells (Table S3), especially the G8f-Li, showed a more significant reduction in R_{SEI} and R_{CT} compared to the bare Li cell after cycling. Specifically, the G8f-Li exhibited the lowest final R_{SEI} (7.59 Ω) and R_{CT} (28.1 Ω), which correlates with the stable voltage profiles observed for over 400 h. This result indicates that the G8f-SEI facilitates the formation of a more stable and ion-conductive interface during cycling, effectively suppressing the continuous impedance growth often seen with unstable interphases and retaining long-term interfacial stability and structural integrity of the G8f-SEI, which might be positively affected by self-assembling ability of G derivatives. It is noted that self-assembly of G-quadruplex has been suggested to facilitate the ion transport efficiency of Li^+-ion batteries and cation-dominant ion conduction by inducing low ion conduction barrier through G-quadruplexes and allowing Li^+ migration through G-quadruplex layers when it was used as solid electrolyte and G8 has a similar structure to LiGQ, which showed high cationic transference number of 0.87 in a symmetric cell due to the facile ion transport characteristics based on ion slippage behavior according to our previous studies [36, 42].

To demonstrate the practical viability of our G8f-SEI, we evaluated its performance in commercial-level Li-metal battery (LMB) full-cells (Figure S11). The full-cells consist of a high-loading NCM811 cathode (3.6 mAh cm^{-2}) and a thin Li-metal anode (20 μm) coated with G8f. Notably, even under a high discharge current density of 3.6 mA cm^{-2} (corresponding to 1C rate) and a high discharge capacity of 3.6 mAh cm^{-2}, the G8f-Li cell exhibited significantly improved cycling stability and lower voltage polarization compared to the bare Li cell. These results suggest that the G8f-based artificial SEI maintains good structural integrity and ion-conducting capability even under high-rate scenarios required for practical batteries.

The morphological changes in Li after the cycle test were also investigated using a scanning electron microscope (Figure 6a and Figure S12). Several needle-like Li dendrites and dead Li were formed on bare Li after the cycle test (Figure S12) with severe volume expansion and dead Li formation, whereas every artificial

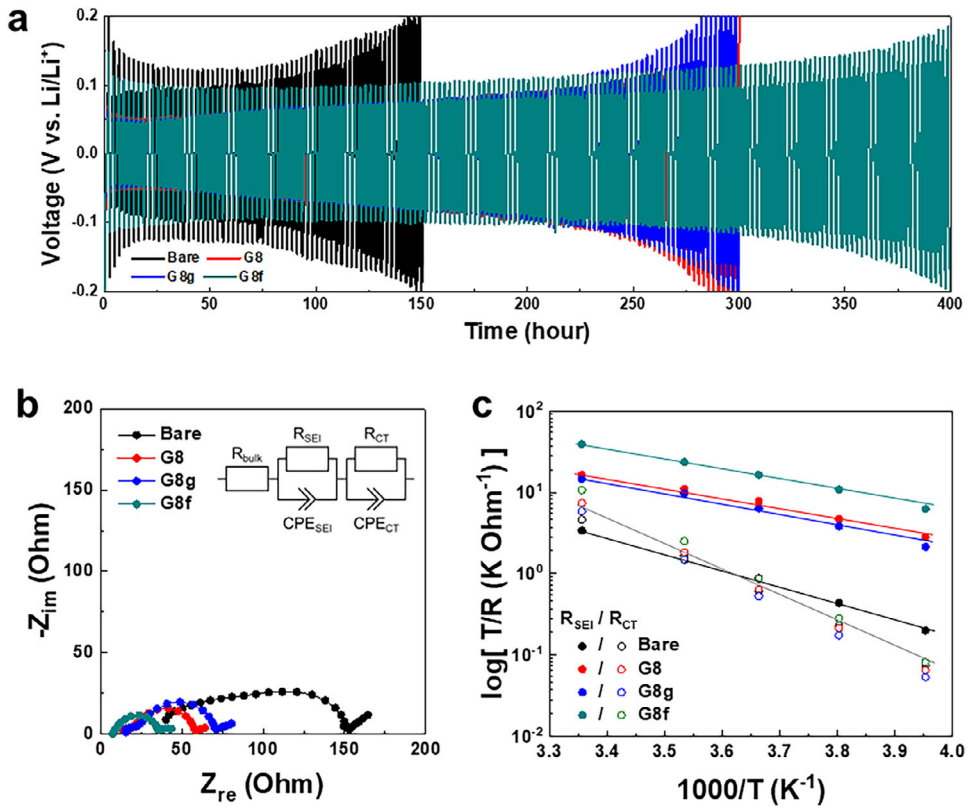

FIGURE 5 | Application to artificial SEI for Li metal anodes. (a) Voltage profiles of Li|Li symmetric cells with artificial SEIs (G8g, G8, G8f), comparing that of bare Li. (b) Electrochemical Impedance spectroscopy (EIS) profiles of the Li|Li symmetric cells after the cycle test. Inset is a corresponding equivalent circuit model of the Li metal anode. (c) Arrhenius plots of R_{SEI} and R_{CT} of the Li|Li symmetric cells after the cycle test.

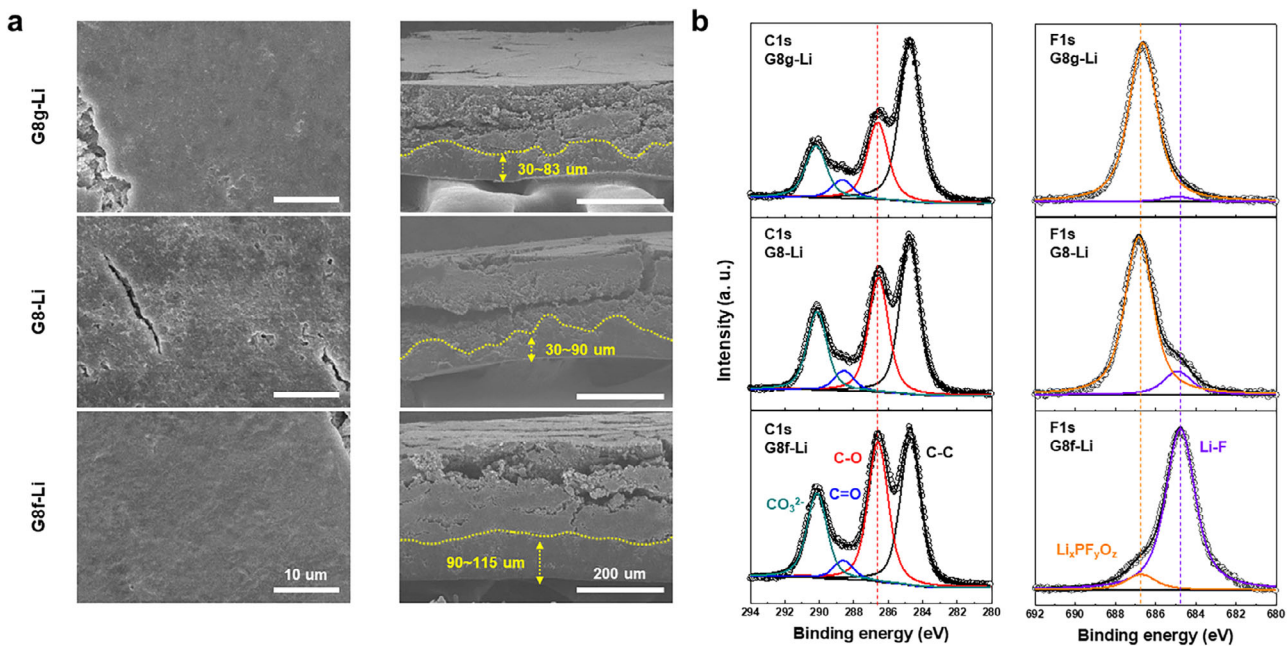

FIGURE 6 | Morphological change of the Li metal after the cycle test. (a) Surface (left) and cross-sectional (right) scanning electron microscope (SEM) images of the Li metal anodes after the cycle test. (b) X-ray photoelectron microscopy (XPS) C1s (left) and F1s (right) spectra of the Li metal anodes after the cycle test.

SEI-containing Li exhibited a denser active Li layer compared to bare Li. These phenomena indicate that artificial SEIs substantially suppress the formation of Li dendrites (left images in Figure 6a), improving lithium utilization efficiency. In addition, G8f-Li maintains the thickest active Li layer on the bottom side (right images in Figure 6a). These results suggest that the high structural integrity of the G8f together with its strong tendency to form highly ordered self-assembled structures, may contribute to reversible utilization of active Li. This behavior may be related to potentially favorable ion transfer pathways within the self-assembled layers [36, 42]. To elucidate this interfacial behavior in more detail, the chemical composition of Li was analyzed by X-ray photoelectron microscopy (Figure 6b and Figure S13a) because our molecules are composed of light elements, such as C, O, N, and F, which are hard to detect with standard EDX with X-rays with low energy and easily absorbed by the sample itself or by the detector's window, and thereby the accuracy and reliability are limited. The C1s spectra show that bare Li and artificial SEI-containing Li contain typical carbonaceous species (C1s spectra in Figure 6b and Figure S13a), which originate from the decomposition of carbonates in the liquid electrolytes [40]. In contrast, the major differences lie in the significant variation in the inorganic F content in these interphases (F1s spectra in Figure 6b and Figure S13b). The bare Li shows $Li_xPF_yO_z$ peak from the salt and Li–F peak from salt decomposition after cycle test, and introduction of G8g and G8 as SEI to Li reduces electrolyte decomposition and lowers Li–F fractions compared to $Li_xPF_yO_z$ fractions. On the other hand, G8f-Li showed the intense Li-F peak compared to $Li_xPF_yO_z$ after cycle test although the coverage is fair enough. This indicates that some fluoroalkyl chains in G8f participate in forming a LiF-rich interphase and amount of the Li–F peak formed by interaction between Li and fluoroalkyl chains in G8f becomes dominant over the original Li salt peak and Li–F peak from salt decomposition on the surface of Li metal anode. It is reported that the formation of Li–F at SEI–Li interface could contributed to interfacial stabilization of the SEI and suppresses the volume expansion of Li and the direct exposure of native Li to the electrolyte, which is consistent with the enhanced cyclability of G8f compared to that of G8 in Figure 5a [43, 44]. Furthermore, polymer-alloy-fluoride interphase and redistribution of fluoride in Li metal batteries are also reported as important factors to consider to design SEI design to enable fast ion transport kinetics and enhance stability [45–47]. The unique interphase of the fluoroalkyl side chain plays an important role in enabling the interfacial stabilization of Li.

3 | Conclusions

Newly discovered shapes of G self-assemblies are herein reported by incorporating alkyl (G8), fluoroalkyl (G8f), and oligoether (G8g) chains into the G moiety. The STM results and calculations show that the presence and type of the side chain strongly affect the G self-assembly network, resulting in unordered frameworks for G and G8g and highly ordered quartet and hexad self-assembled nanostructures for G8 and G8f, respectively. The usability of the favorable self-assembling ability of G derivatives was highlighted by their application as artificial SEIs in Li metal battery electrodes, where the G8f-Li cell exhibited a higher mechanochemical stability and better efficient ion transport than the other G derivative-based Li cells, which could be attributed to favorable self-assembling ability and rigid structural integrity. Our study highlights that simple side-chain engineering can control the self-assembly of nanostructures and provide a useful strategy for designing artificial SEIs for Li metal batteries and related supramolecular systems, where shape control of supramolecular structures is crucial to device performance.

4 | Experimental Section

4.1 | STM Experiments

STM experiments were performed using a UHV JT STM (SPECS, USA) at 4.4 K. We prepared an Au(111) single crystal with multiple cycles of Ar^+ sputtering and annealing at 780 K as a substrate. After confirming that the Au(111) surface was clean, G and its derivatives (G8, G8f, and G8g) were deposited in a preparation chamber at room temperature. Each molecule was evaporated from a resistively heated Ta boat, with the boat temperature maintained at 250–280°C. The surface coverage of the molecules, which ranged from sub-monolayer to multilayer, was controlled by adjusting the deposition time between 3 and 50 min, depending on the molecule and desired coverage. For multilayer deposition of G8f was prepared by depositing at 280°C for 50 min. The chamber pressure during deposition remained at $\approx 4 \times 10^{-9}$ Torr.

4.2 | Thin-Film Microstructure Analyses

Samples for thin-film microstructure analyses were prepared by thermal evaporation of G and its derivatives on Si substrate (under high vacuum of 1.5×10^{-6} torr and moderate temperatures of 180–200°C range). The measurement of GIXD data was acquired at PLS-II 6D UNIST-PAL beamline of Pohang Accelerator Laboratory in Korea. An X-ray beam at 11.015 keV (λ = 1.12556 Å) was obtained by monochromating the X-rays coming from the in-vacuum undulator (IVU) using a double crystal monochromator. The X-ray beam was irradiated at an incidence angle of 0.12° for 45–100 s. The GIXD patterns were recorded using a 2D charge-coupled device detector with a sample-to-detector distance of 165.4 mm.

4.3 | Structural Characterizations

The surface and cross-sectional morphologies of the Li electrodes were characterized using a field-emission scanning electron microscope (FE-SEM, S-4800 (Hitachi)). The chemical species formed on the SEI of the cycled Li electrodes were investigated using X-ray photoelectron spectroscopy (XPS, K-alpha (Thermo Fisher)).

4.4 | Electrochemical Analysis

Electrochemical performance was investigated using a 2032-type coin cell and a potentiostat (VSP classic, (Bio-Logic)). A liquid electrolyte (1 M $LiPF_6$ in ethylene carbonate/diethyl carbonate = 1/1 (v/v)) without additives was used. The Li metal anode cycle test was conducted with the Li|Li symmetric cell under a current density of 1 mA cm^{-2} for 1 h per cycle at room

temperature. Interfacial resistance analysis was performed using electrochemical impedance spectroscopy in the frequency range of 10^{-2}–10^{6} Hz, an applied amplitude of 10 mV, and various temperature conditions.

4.5 | Thermal Evaporation Method of G Derivatives for Battery Application

For the application in a Li metal battery system as an artificial SEI, a 100 nm thick film of G and its derivatives were thermally deposited on Li foil (under high vacuum of 1.5×10^{-6} torr and at moderate temperature in the range of 180–200°C).

More detailed information of synthesis and calculation is provided in Supporting Information.

Acknowledgements

This work was supported by Samsung Research Funding Center of Samsung Electronics under Project Number SRFC-MA1702-04 and the Nano & Material Technology Development Program through the National Research Foundation of Korea (NRF) funded by Ministry of Science and ICT (RS-2025-25442266) (50% contribution to this work). We thank UNIST Office of Research Facilities and Training (ResFacT) for support of using the equipment. Computational resources are supported by KISTI (KSC-2024-CRE-0143) and UNIST-HPC. 2D-GIXD experiments were performed at PLS-II 3C SAXS I, 9A U-SAXS, and 6D UNIST-PAL beamlines of Pohang Accelerator Laboratory in Korea.

Conflicts of Interest

The authors declare no conflicts of interest.

Data Availability Statement

The data that support the findings of this study are available from the corresponding author upon reasonable request.

References

1. K. Hoogsteen, "The Structure of Crystals Containing a Hydrogen-Bonded Complex of 1-Methylthymine and 9-Methyladenine," *Acta Crystallographica* 12 (1959): 822–823, https://doi.org/10.1107/S0365110X59002389.

2. W. Traub and J. L. Sussman, "Adenine-Guanine Base Pairing in Ribosomal RNA," *Nucleic Acids Research* 10 (1982): 2701–2708, https://doi.org/10.1093/nar/10.8.2701.

3. V. B. Zhurkin, M. Y. Tolstorukov, F. Xu, A. V. Colasanti, and W. K. Olson, "Sequence-Dependent Variability of B-DNA," in *DNA Conformation and Transcription* (Springer, 2005), 18–34, https://doi.org/10.1007/0-387-29148-2.

4. K. L. Arthur, G. A. Eiceman, J. C. Reynolds, and C. S. Creaser, "Analysis of Supramolecular Complexes of 3-Methylxanthine with Field Asymmetric Waveform Ion Mobility Spectrometry Combined with Mass Spectrometry," *Journal of the American Society for Mass Spectrometry* 27 (2016): 800–809, https://doi.org/10.1007/s13361-016-1351-y.

5. J. Novotný, P. Kulhánek, and R. Marek, "Biocompatible Xanthine-Quadruplex Scaffold for Ion-Transporting DNA Channels," *The Journal of Physical Chemistry Letters* 3 (2012): 1788–1792, https://doi.org/10.1021/jz300559w.

6. J. Novotný, Y. P. Yurenko, P. Kulhánek, and R. Marek, "Tailoring the Properties of Quadruplex Nucleobases for Biological and Nanomaterial Applications," *Physical Chemistry Chemical Physics* 16 (2014): 15241–15248, https://doi.org/10.1039/C4CP00541D.

7. J. Szolomájer, G. Paragi, G. Batta, et al., "3-Substituted Xanthines as Promising Candidates for Quadruplex Formation: Computational, Synthetic and Analytical Studies," *New Journal of Chemistry* 35 (2011): 476–482, https://doi.org/10.1039/C0NJ00612B.

8. Y. P. Yurenko, J. Novotný, V. Sklenář, and R. Marek, "Exploring Non-covalent Interactions in Guanine- and Xanthine-Based Model DNA Quadruplex Structures: a Comprehensive Quantum Chemical Approach," *Physical Chemistry Chemical Physics* 16 (2014): 2072–2084, https://doi.org/10.1039/C3CP53875C.

9. A. Ciesielski, S. Haar, A. Bényei, et al., "Self-Assembly of N 3 -Substituted Xanthines in the Solid State and at the Solid–Liquid Interface," *Langmuir* 29 (2013): 7283–7290, https://doi.org/10.1021/la304540b.

10. A. Calzolari, R. Di Felice, E. Molinari, and A. Garbesi, "Self-Assembled Guanine Ribbons as Wide-Bandgap Semiconductors," *Physica E: Low-Dimensional Systems and Nanostructures* 13 (2002): 1236–1239, https://doi.org/10.1016/S1386-9477(02)00343-0.

11. G. N. M. Reddy, A. Marsh, J. T. Davis, S. Masiero, and S. P. Brown, "Interplay of Noncovalent Interactions in Ribbon-Like Guanosine Self-Assembly: An NMR Crystallography Study," *Crystal Growth & Design* 15 (2015): 5945–5954, https://doi.org/10.1021/acs.cgd.5b01440.

12. G. Paragi, "Cooperativity in the Self-Assembly of the Guanine Nucleobase into Quartet and Ribbon Structures on Surfaces," *Chemistry—A European Journal* 23 (2017): 3042–3050, https://doi.org/10.1002/chem.201604830.

13. L. Stefan and D. Monchaud, "Applications of Guanine Quartets in Nanotechnology and Chemical Biology," *Nature Reviews Chemistry* 3 (2019): 650–668, https://doi.org/10.1038/s41570-019-0132-0.

14. C. Zhang, L. Xie, L. Wang, H. Kong, Q. Tan, and W. Xu, "Atomic-Scale Insight into Tautomeric Recognition, Separation, and Interconversion of Guanine Molecular Networks on Au(111)," *Journal of the American Chemical Society* 137 (2015): 11795–11800, https://doi.org/10.1021/jacs.5b07314.

15. N. Huang, P. Wang, and D. Jiang, "Covalent Organic Frameworks: A Materials Platform for Structural and Functional Designs," *Nature Reviews Materials* 1 (2016): 16068, https://doi.org/10.1038/natrevmats.2016.68.

16. K. Geng, T. He, R. Liu, et al., "Covalent Organic Frameworks: Design, Synthesis, and Functions," *Chemical Reviews* 120 (2020): 8814–8933, https://doi.org/10.1021/acs.chemrev.9b00550.

17. S. Cao, B. Li, R. Zhu, and H. Pang, "Design and Synthesis of Covalent Organic Frameworks towards Energy and Environment Fields," *Chemical Engineering Journal* 355 (2019): 602–623, https://doi.org/10.1016/j.cej.2018.08.184.

18. R. Lin, Y. He, P. Li, H. Wang, W. Zhou, and B. Chen, "Multifunctional Porous Hydrogen-Bonded Organic Framework Materials," *Chemical Society Reviews* 48 (2019): 1362–1389, https://doi.org/10.1039/C8CS00155C.

19. Q. Wang and D. Astruc, "State of the Art and Prospects in Metal–Organic Framework (MOF)-Based and MOF-Derived Nanocatalysis," *Chemical Reviews* 120 (2020): 1438–1511, https://doi.org/10.1021/acs.chemrev.9b00223.

20. T. Lei, J. Wang, and J. Pei, "Roles of Flexible Chains in Organic Semiconducting Materials," *Chemistry of Materials* 26 (2014): 594–603, https://doi.org/10.1021/cm4018776.

21. J. Mei and Z. Bao, "Side Chain Engineering in Solution-Processable Conjugated Polymers," *Chemistry of Materials* 26 (2014): 604–615, https://doi.org/10.1021/cm4020805.

22. B. Meng, J. Liu, and L. Wang, "Oligo(ethylene glycol) as Side Chains of Conjugated Polymers for Optoelectronic Applications," *Polymer Chemistry* 11 (2020): 1261–1270, https://doi.org/10.1039/C9PY01469A.

23. C. Chen, S. Wang, S. Tung, and W. Su, "Oligo(Ethylene Glycol) Side Chain Effect on the Physical Properties and Molecular Arrangement of

Oligothiophene–Isoindigo Based Conjugated Polymers," *Soft Matter* 15 (2019): 9468–9473, https://doi.org/10.1039/C9SM01471C.

24. B. Kang, Z. Wu, M. J. Kim, H. Y. Woo, and J. H. Cho, "Aqueous-Alcohol-Processable High-Mobility Semiconducting Copolymers with Engineered Oligo(ethylene glycol) Side Chains," *Chemistry of Materials* 32 (2020): 1111–1119, https://doi.org/10.1021/acs.chemmater.9b04004.

25. S. Yang, X. Zhang, P. Chen, et al., "Diketopyrrolopyrrole-Based Semiconducting Polymer with both Hydrophobic Alkyl and Hydrophilic Tetraethylene Glycol Chains for Monolayer Transistor and Sensing Application," *Advanced Electronic Materials* 3 (2017): 1700120, https://doi.org/10.1002/aelm.201700120.

26. A. Giovannitti, I. P. Maria, D. Hanifi, et al., "The Role of the Side Chain on the Performance of N-Type Conjugated Polymers in Aqueous Electrolytes," *Chemistry of Materials* 30 (2018): 2945–2953, https://doi.org/10.1021/acs.chemmater.8b00321.

27. E. Lee, B. Hammer, J. Kim, Z. Page, T. Emrick, and R. C. Hayward, "Hierarchical Helical Assembly of Conjugated Poly(3-hexylthiophene)-block-poly(3-triethylene glycol thiophene) Diblock Copolymers," *Journal of the American Chemical Society* 133 (2011): 10390–10393, https://doi.org/10.1021/ja2038547.

28. B. Kang, R. Kim, S. B. Lee, S. Kwon, Y. Kim, and K. Cho, "Side-Chain-Induced Rigid Backbone Organization of Polymer Semiconductors through Semifluoroalkyl Side Chains," *Journal of the American Chemical Society* 138 (2016): 3679–3686, https://doi.org/10.1021/jacs.5b10445.

29. B. Wang, S. Watt, M. Hong, et al., "Synthesis, Properties, and Tunable Supramolecular Architecture of Regioregular Poly(3-alkylthiophene)s with Alternating Alkyl and Semifluoroalkyl Substituents," *Macromolecules* 41 (2008): 5156–5165, https://doi.org/10.1021/ma702408h.

30. H. E. Katz, A. J. Lovinger, J. Johnson, et al., "A Soluble and Air-Stable Organic Semiconductor with High Electron Mobility," *Nature* 404 (2000): 478–481, https://doi.org/10.1038/35006603.

31. R. T. Weitz, K. Amsharov, U. Zschieschang, et al., "Organic n-Channel Transistors Based on Core-Cyanated Perylene Carboxylic Diimide Derivatives," *Journal of the American Chemical Society* 130 (2008): 4637–4645, https://doi.org/10.1021/ja074675e.

32. K. Xu, "Electrolytes and Interphases in Li-Ion Batteries and beyond," *Chemical Reviews* 114 (2014): 11503–11618, https://doi.org/10.1021/cr500003w.

33. J. Liu, Z. Bao, Y. Cui, et al., "Pathways for Practical High-Energy Long-Cycling Lithium Metal Batteries," *Nature Energy* 4 (2019): 180–186, https://doi.org/10.1038/s41560-019-0338-x.

34. D. Lin, Y. Liu, and Y. Cui, "Reviving the Lithium Metal Anode for High-Energy Batteries," *Nature Nanotechnology* 12 (2017): 194–206, https://doi.org/10.1038/nnano.2017.16.

35. X. Cheng, R. Zhang, C. Zhao, and Q. Zhang, "Toward Safe Lithium Metal Anode in Rechargeable Batteries: A Review," *Chemical Reviews* 117 (2017): 10403–10473, https://doi.org/10.1021/acs.chemrev.7b00115.

36. S. Cho, K. M. Lee, S. Kang, et al., "Ion Slippage through Li^+-Centered G-Quadruplex," *Science Advances* 8 (2022): abp8751, https://doi.org/10.1126/sciadv.abp8751.

37. R. Otero, M. Schöck, L. M. Molina, et al., "Guanine Quartet Networks Stabilized by Cooperative Hydrogen Bonds," *Angewandte Chemie International Edition* 44 (2005): 2270–2275, https://doi.org/10.1002/anie.200461586.

38. Y. Ding, L. Xie, D. Li, H. Shen, C. Li, and W. Xu, "Interconversion between Guanine Quartets and Triads on the Au(111) Surface," *Chemical Communications* 58 (2022): 3198–3201, https://doi.org/10.1039/D2CC00060A.

39. F. Rossel, P. Brodard, F. Patthey, N. V. Richardson, and W. Schneider, "Modified Herringbone Reconstruction on Au(111) Induced by Self-Assembled Azure A Islands," *Surface Science* 602 (2008): L115–L117, https://doi.org/10.1016/j.susc.2008.06.009.

40. D. Lu, Y. Shao, T. Lozano, et al., "Failure Mechanism for Fast-Charged Lithium Metal Batteries with Liquid Electrolytes," *Advanced Energy Materials* 5 (2015): 1400993, https://doi.org/10.1002/aenm.201400993.

41. C. Fang, J. Li, M. Zhang, et al., "Quantifying Inactive Lithium in Lithium Metal Batteries," *Nature* 572 (2019): 511–515, https://doi.org/10.1038/s41586-019-1481-z.

42. S. Kang, K. M. Lee, S. Cho, et al., "Guanine-Based G-Quadruplexes Templated by Various Cations toward Potential Use as Single-Ion Conductors," *Chemsuschem* 15 (2022): 202102201, https://doi.org/10.1002/cssc.202102201.

43. L. Suo, W. Xue, M. Gobet, et al., "Fluorine-Donating Electrolytes Enable Highly Reversible 5-V-Class Li Metal Batteries," *Proceedings of the National Academy of Sciences* 115 (2018): 1156–1161, https://doi.org/10.1073/pnas.1712895115.

44. J. Chen, X. Fan, Q. Li, et al., "Electrolyte Design for LiF-Rich Solid–Electrolyte Interfaces to Enable High-Performance Microsized Alloy Anodes for Batteries," *Nature Energy* 5 (2020): 386–397, https://doi.org/10.1038/s41560-020-0601-1.

45. G. Li, X. Duan, X. Liu, et al., "Locking Active Li Metal through Localized Redistribution of Fluoride Enabling Stable Li-Metal Batteries," *Advanced Materials* 35 (2023): 2207310, https://doi.org/10.1002/adma.202207310.

46. Y. Li, E. Mao, Z. Min, et al., "Hybrid Polymer-Alloy-Fluoride Interphase Enabling Fast Ion Transport Kinetics for Low-Temperature Lithium Metal Batteries," *ACS Nano* 17 (2023): 19459–19469, https://doi.org/10.1021/acsnano.3c08576.

47. Y. Li, S. Kumar, G. Yang, et al., "The Contrast between Monovalent and Multivalent Metal Battery Anodes," *Science* 389 (2025): adl5482, https://doi.org/10.1126/science.adl5482.

Supporting Information

Additional supporting information can be found online in the Supporting Information section.

Supporting File: adfm74961-sup-0001-SuppMat.docx.